Computer simulation of wound closure in epithelial tissues: Cell–basal-lamina adhesion

Tatsuzo Nagai[1] and Hisao Honda[2]
[1]*Research Center, Kyushu Kyoritsu University, Kitakyushu, Fukuoka 807-8585, Japan*
[2]*Hyogo University, Kakogawa, Hyogo 675-0195, Japan*
(Received 28 July 2009; revised manuscript received 25 October 2009; published 9 December 2009)

The mechanism of wound closure in epithelial tissues, i.e., cell monolayer sheets, is investigated through computer simulations. A wound means an area in which some cells have been removed from the normal tissue. The vertex dynamics cell model [T. Nagai and H. Honda, Philos. Mag. B **81**, 699 (2001)], which describes morphogenesis of epithelial tissues using the concepts of statistical physics, is modified and applied to the closure of small wounds without mitosis. It is shown that cell–basal-lamina adhesion governs the wound closure competing with cell-cell adhesion and cell elasticity. The simulation results reproduce the actual wound closure process qualitatively and partly quantitatively. The closing proceeds with the translation of the edges of wound polygons toward the wound center and the intermittent reduction in the number of polygon edges. Over time, the process leads to an exponential decrease in the wound area. A shape factor is introduced to describe the wound shape quantitatively and is used to examine the time variation thereof. A method for determining model parameters by comparison with the experiments is given.

DOI: 10.1103/PhysRevE.80.061903 PACS number(s): 87.17.Pq, 87.19.lx, 87.18.Gh, 87.17.Rt

I. INTRODUCTION

The spread of epithelial cell sheets plays a central role in the early stage of multicellular animal morphogenesis and has been investigated by observing wound closure. Past studies of the wound closure can be classified using the length scale of each subject. The first classification includes molecule-level studies that focus on biochemical substances and their functions concerned with the wound closure. This has been the main focus of wound closure studies in the past [1]. The second includes cell-level studies which focus on the mechanical structure of cell movements around wounds [2–7]. The final classification is for cell-assembly-level studies that describe cell assemblies as continuums to obtain space-time structures of cell density. Due to the universality of mathematical models since early times, these studies have covered a wide range of fields [8–13].

The purpose of this paper is to clarify the mechanism of wound closure at the cell level. In other words, we aim to find the whole picture of wound closure in terms of cells as the basic elements in the entire system encompassing the wound area, the cells surrounding the wound, basal lamina touching the cellular bases, and an environmental medium.

We now discuss experimental studies relevant to our aim. The behavior of an isolated rat hepatocyte on a serum-pretreated glass surface was observed using a scanning electron microscope [2,5]. The photographs thus obtained show that the hepatocyte spreads out radially in a concentric circle and then gradually flattens. The hepatocyte behaves like a liquid drop wetting a solid surface.

Epidermal cell movements during closure of a wound, caused by removing approximately ten cells from the normal tissue of a *Xenopus laevis* tadpole fin, were filmed directly using time-lapse cinemicrography, since a tadpole fin is transparent, flat, and thin [3]. The consecutive pictures show that, during the process of wound closure, marginal cells cover the wound from the lateral sides and that the wound contracts approximately retaining its initial shape.

Cell movements in wounded cat corneal endothelia, in which about 180 cells were removed from the normal tissue, were observed directly for an extended time [4]. Circumferential cells around the wound flow into the wound like a two-dimensional fluid and cover the wound. In this process the cells do not proliferate, but various changes in the cells, such as elongation, contraction, transfer of the center of gravity, exchange of positions, increase in the area and so forth, are deemed to come from the contractility of actin filaments.

Three protein filaments, namely, actin filaments, microtubules, and intermediate filaments, generally known as the cytoskeleton in a cell of a multicellular animal, yield the elasticity of a cell needed to resist external forces. Their viscoelasticities were measured using rheologic methods *in vitro* and the stress-strain curves obtained thereof [14]. The results show that the three filaments each have their own elastic range of stress and that the actin filament has the widest elastic range and the smallest strain for the same stress. This leads to the conclusion that actin filaments play a central role in sustaining the shape of a cell.

A histological study of wound closure in *Xenopus laevis* embryos has recently been performed using videomicroscopy [6,7]. The time change of the shape of a wound was recorded resulting in a graph of the time dependence of the wound area. The authors also found discontinuous accumulation of actin filaments along the closing wound edges. Further investigation of the morphology of the epidermis along the wound edges with a scanning electron microscope revealed that the epidermal cells elongated significantly toward the wound and that the wound edges were not smoothed, but remained ragged during the wound closure, contrary to the effect of contractile actin cables. These observations led to the conclusion that the wound closure in *Xenopus laevis* embryos may be driven by a more complex mechanism that involves not only the contractility mechanism of actin filaments, the so-called actin "purse string," but also inward movements of individual cells maintaining cell-cell contacts.

Previously, we proposed a model, the vertex dynamics cell model, which describes the morphogenesis of normal epithelial tissue, that is, cell-monolayer sheets without wound [15]. In this model each cell is represented by a right prism and thus the whole system of epithelial tissue can be described in terms of an assembly of polygonal vertices in apical surfaces of the prisms. These vertices are driven by thermodynamic forces to minimize the total potential energy of the system and at the same time they receive viscous resistance leading to dissipative motions. The total potential energy of the system consists of interfacial energies at the cell-cell boundaries and elastic energies of the cell volume. We performed computer simulations using this model and found that the system eventually forms a kind of honeycomb pattern, or tortoise-shell pattern, despite starting from various initial states. This result confirms that this kind of honeycomb pattern of cells is ubiquitous in the epithelial tissue of many species.

As candidates for the driving force of wound closure, we compared cell-wound interfacial energy with cell–basal-lamina interfacial energy. The basal lamina is a soft thin mat on which epithelial cells rest and which separates the epithelial cells from the connective tissue [16]. The former gives the contractility mechanism of actin filaments to the wound contour, while the latter gives the new mechanism of cell–basal-lamina adhesion which describes the spreading of an isolated rat hepatocyte on a serum-pretreated glass surface as mentioned above. We performed computer simulations and found that the former alone could not reproduce the two experimental results within reasonable parameter ranges, which are that a wound contracts while almost retaining its initial shape and that a wound eventually closes completely. In fact, there is a strong tendency for the cell-wound interfacial tension to make the wound circular during the wound contraction process. In addition, if the coefficient of the tension is smaller than that of the cell-cell interfacial tension, the wound expands, otherwise it contracts, which is unreasonable from the viewpoint that the tension originates from the actin filaments in each cell. Therefore, in this paper we introduce cell–basal-lamina interfacial energy into the vertex dynamics cell model as the primary driving force of wound closure and cell-wound interfacial energy as the secondary force, and perform appropriate computer simulations [17]. It should be noted that in this paper we focus on the closure of small wounds by cell spreading and cell rearrangement and that mitotic processes are not included in the simulations.

II. VERTEX DYNAMICS CELL MODEL OF WOUND CLOSURE

In order to treat wound closure, we add two elements, namely, a cell–basal-lamina adhesive force and the disappearance process of the wound, to the vertex dynamics cell model [15]. As mentioned in the preceding section, we represent each cell approximately by a right prism, coarse graining a real cell with a small length scale Δ, which is the minimum length in the model and much smaller than the average radius of cells. Then we can represent epithelial tissue using a set of two-dimensional vectors of vertex positions, $\{\boldsymbol{r}_i\}$, forming individual apical surfaces of prisms and a set of cell heights, $\{h_i\}$. Here we assume that three cell boundaries radiate from each vertex to connect with three neighboring vertices.

A. Equations of motion for vertices

We adopt the completely dissipative equations of motion for vertices that have been applied to many interface systems, e.g., various foams, emulsions, and crystalline grains [15,18]. The time change of the positional vector of vertex i, $\boldsymbol{r}_i$, is then given by

$$\eta \frac{d\boldsymbol{r}_i}{dt} = -\frac{\partial}{\partial \boldsymbol{r}_i} U, \tag{1}$$

where η denotes the coefficient of viscous resistance and U the total potential energy of the system. Equation (1) expresses the balance of the dissipative force on the left-hand side and the potential force on the right-hand side and guarantees that all vertices move in such a way as to decrease U [15]. The total potential energy of the system is assumed to be

$$U = U_{\mathrm{I}} + U_{\mathrm{D}} + U_{\mathrm{B}}, \tag{2}$$

where U_{I} is the cell-cell and cell-wound lateral-interfacial energy, U_{D} is the elastic energy of cells, and U_{B} is the cell–basal-lamina interfacial energy.

U_{I} is expressed by

$$U_{\mathrm{I}} = \sum_{\langle ij \rangle} \sigma_{\langle ij \rangle} r_{ij}, \tag{3}$$

where $r_{ij} \equiv |\boldsymbol{r}_{ij}| \equiv |\boldsymbol{r}_i - \boldsymbol{r}_j|$, and $\sigma_{\langle ij \rangle}$ is the interfacial potential energy density of the straight boundary $\langle ij \rangle$, equal to σ for cell-cell boundaries and σ^{F} for cell-wound boundaries.

Denoting the area of cell α by S_α and its equilibrium value by S_α^0, U_{D} is written as

$$U_{\mathrm{D}} = \sum_{\alpha}^{(\mathrm{cell})} \rho (h^0)^2 (S_\alpha - S_\alpha^0)^2, \tag{4}$$

where ρ is a positive constant and h^0 an equilibrium cell height, both of which are assumed to be independent of the cell. The equilibrium value of cell area S_α^0 is given by

$$S_\alpha^0 = \frac{1}{1 + n_\alpha^{\mathrm{C}}} \left(S_\alpha + \sum_{\beta=1}^{n_\alpha^{\mathrm{C}}} S_\beta \right), \tag{5}$$

where n_α^{C} is the number of cells surrounding cell α, not always the edge number of cell α [15]. Equation (5) means that S_α^0 equals the average area of cells over cell α and its n_α^{C} neighbors, β, and thus depends on time, assuming a local equilibrium.

In Sec. I, we discussed an experimental result in which an isolated rat hepatocyte spreads out on a serum-pretreated glass surface like a liquid drop wetting a solid surface. A liquid drop in such a wetting phenomenon causes decrease in the total interfacial energy by covering a solid surface. This analogy leads us to the assumption that cells cover wounds

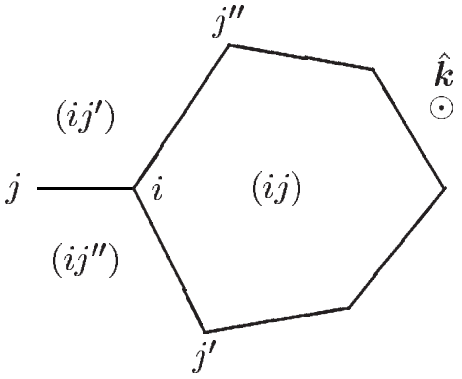

FIG. 1. Neighbor vertices (j,j',j'') and neighbor cells (ij,ij',ij'') of vertex i.

with the purpose of decreasing the total interfacial energy and subsequently to the expression of potential energy of wounds given by

$$U_{\mathrm{B}} = \sum_{\gamma}^{(\mathrm{wound})} \sigma^{\mathrm{B}} S_{\gamma}^{\mathrm{F}}, \tag{6}$$

where σ^{B} is a positive constant and S_{γ}^{F} is the area of wound γ.

U_{I} and U_{D} give rise to the main forces which preside over the morphogenesis of epithelial tissues [15]. U_{I} produces the forces that contract cell boundaries and U_{D} the forces that maintain individual cell areas around their equilibrium values. Substituting Eqs. (3) and (4) into Eq. (1) we obtain their explicit forms as

$$\boldsymbol{f}_i^{\mathrm{I}} = -\sum_{j}^{(i)} \sigma_{ij',ij''} \frac{\boldsymbol{r}_{ij}}{r_{ij}} \tag{7}$$

and

$$\boldsymbol{f}_i^{\mathrm{D}} = -\sum_{j}^{(i)} \rho (h^0)^2 (S_{ij} - S_{ij}^0) \boldsymbol{r}_{j'j''} \times \hat{\boldsymbol{k}}. \tag{8}$$

In Eqs. (7) and (8), three vertices (j,j',j'') connected to vertex i via cell boundaries (cell-cell or cell-wound), which are hereafter called neighbor vertices, are defined in an anticlockwise order around vertex i and the three cells surrounding vertex i are expressed as $(ij),(ij'),(ij'')$, as shown in Fig. 1. The unit vector $\hat{\boldsymbol{k}}$ is perpendicular to the surface of the paper and points from the back to the face of the paper as shown in Fig. 1.

U_{B} produces the primary driving force for wound closure. When wound γ appears with an area S_{γ}^{F}, the potential energy increases by $\sigma^{\mathrm{B}} S_{\gamma}^{\mathrm{F}}$ and thus the marginal cells along the wound-cell boundaries tend to lessen the increment by covering the wound. The movement of the marginal cells, however, generally causes an increase in both U_{I} and U_{D}. As a result, competition among them determines whether the wound closure advances or stagnates. Substituting Eq. (6) into Eq. (1), the force acting on vertex i on the wound-cell boundary is explicitly given by

$$\boldsymbol{f}_i^{\mathrm{B}} = -\frac{\sigma^{\mathrm{B}}}{2} \boldsymbol{r}_{j'j''} \times \hat{\boldsymbol{k}}, \tag{9}$$

where $\boldsymbol{r}_{j'j''} \equiv \boldsymbol{r}_{j'} - \boldsymbol{r}_{j''}$. The three vertices (i,j',j'') in Eq. (9) are arranged in an anticlockwise order along the wound margin viewing the wound region on the left as shown in Fig. 1 with wound (ij). It should be noted that the force defined in Eq. (9) always points toward the wound and has a magnitude proportional to $|\boldsymbol{r}_{j'j''}|$.

B. Elementary processes of topological changes

In addition to the equations of motion for vertices Eq. (1), we also introduce the following three elementary processes, shown in Fig. 2, into our model to describe the topological changes in cellular patterns.

(1) Recombination process (T1): when two neighbor vertices i and j are within the minimum distance Δ of each other, they partially change the relationships with their neighbor vertices as shown in Fig. 2(a). They rotate the minimum edge ij clockwise by 90° around its midpoint and change the neighbor vertices of vertex i from (j,j',j'') to (j,k',j') and those of vertex j from (i,k'',k') to (i,j'',k'') as shown in Fig. 2(a).

(2) Disappearance process (T2): when the minimum edge ij of a triangular wound W becomes Δ, wound W disappears

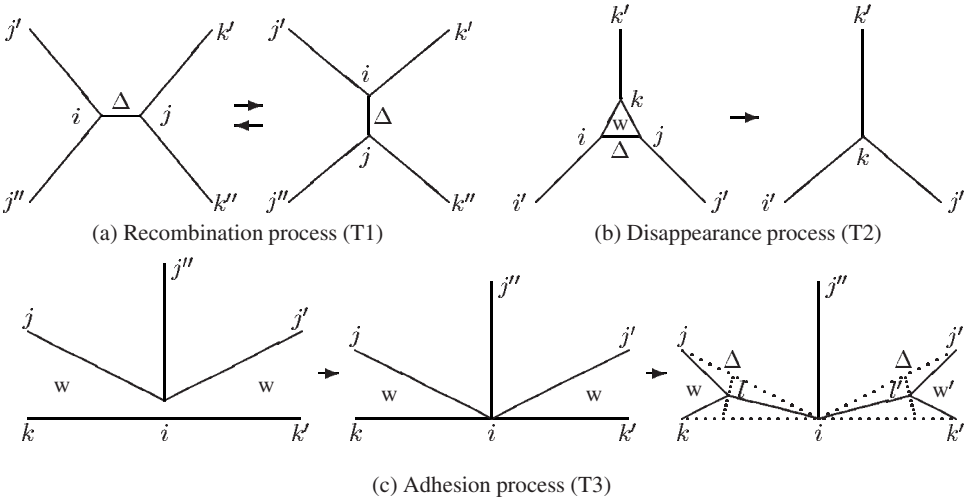

(a) Recombination process (T1)

(b) Disappearance process (T2)

(c) Adhesion process (T3)

FIG. 2. Elementary processes of topological changes in wound closure. (a) Recombination process (T1): changes in relationships between vertices $(i-j'') \rightarrow (i-k')$, $(j-k') \rightarrow (j-j'')$. (b) Disappearance process (T2): disappearance of wound W. (c) Adhesion process (T3): (leftmost, center) vertex i touches another wound edge kk'; (rightmost) three cells adhere to one another and two new vertices l and l' are created where the distances between wound edges defined by the fine dotted lines equal Δ.

and becomes vertex k at the midpoint of edge ij as shown in Fig. 2(b).

(3) Adhesion process (T3): when a vertex on a wound edge touches another wound edge, cells on both sides adhere to each other and two new vertices l and l' are created as shown in Fig. 2(c). The new vertex l is located at the point that is at a distance of $\Delta/[2\tan(\angle kij/2)]$ from vertex i on a bisector of angle $\angle kij$, as shown in the rightmost diagram of Fig. 2(c). This means that when the distance between two wound edges at vertex l, defined below, is smaller than Δ they are regarded as adhering to each other and being a single wound edge. The distance between two wound edges is defined here as the distance between two points where the perpendicular of edge il at vertex l is intersected by two old edges, ij and ik, as depicted by the dotted lines in the rightmost diagram in Fig. 2(c). Another new vertex l' is also similarly created. Although only the recombination process (T1) was previously included in describing the morphogenesis of epithelial tissues [15], we have introduced the disappearance process (T2) and the adhesion process (T3) for describing wound closure.

III. SIMULATIONS

A. Dimensionless physical quantities and parameter values

For the computer simulations, we transform all physical quantities into dimensionless ones by using a length unit $R_0 \equiv \sqrt{S_0}$, where S_0 is the average cell area at $t=0$, and a time unit $\tau_0 \equiv \eta R_0/\sigma$. These new units represent the characteristic length and time of the system as described below. This leads to new dimensionless variables with the symbol tilde $\tilde{}$, such as $\tilde{\boldsymbol{r}}_i \equiv \boldsymbol{r}/R_0$, $\tilde{t} \equiv t/\tau_0, \ldots$, and new dimensionless parameters defined as

$$\tilde{\rho} \equiv \rho(h^0)^2(R_0)^3/\sigma, \quad \tilde{\sigma}^{\mathrm{F}} \equiv \sigma^{\mathrm{F}}/\sigma, \quad \tilde{\sigma}^{\mathrm{B}} \equiv \sigma^{\mathrm{B}}R_0/\sigma, \quad (10)$$

where the energy unit is chosen as $\varepsilon_0 \equiv \sigma R_0$, which is the cell-cell boundary energy per R_0. Then the dimensionless linear density of energy for a straight boundary $\langle ij \rangle$ is given by

$$\tilde{\sigma}_{\langle ij \rangle} \equiv \sigma_{\langle ij \rangle}/\sigma : \tilde{\sigma}_{\langle ij \rangle} = 1 \quad \text{for cell-cell boundaries;}$$

$$\tilde{\sigma}_{\langle ij \rangle} = \tilde{\sigma}^{\mathrm{F}} \quad \text{for cell-wound boundaries.} \quad (11)$$

Using the dimensionless quantities given above, the equations of motion for vertices Eq. (1) become, dropping the symbol tilde $\tilde{}$ for simplicity,

$$\frac{d\boldsymbol{r}_i}{dt} = -\frac{\partial}{\partial \boldsymbol{r}_i}\left[\sum_{\langle ij \rangle}^{(\text{cell-cell})} r_{ij} + \sum_{\langle ij \rangle}^{(\text{cell-wound})} \sigma^{\mathrm{F}} r_{ij} + \sum_{\alpha}^{(\text{cell})} \rho(S_\alpha - S_\alpha^0)^2 + \sum_{\gamma}^{(\text{wound})} \sigma^{\mathrm{B}} S_\gamma^{\mathrm{F}}\right]. \quad (12)$$

We note that the two new units, R_0 and τ_0, are the most fundamental parameters in the vertex dynamics cell model. They were specifically chosen to give no coefficients to the two terms in Eq. (12), i.e., the vertex velocity on the left-hand side and the cell-cell interfacial potential, the first term on the right-hand side. This stems from our viewpoint that the cell-cell interfacial potential force presides over the morphogenesis of epithelial tissues.

The three parameters in Eq. (12), ρ, σ^{F}, and σ^{B}, were chosen in the following way for our computer simulations. Since ρ is the bulk elastic coefficient of a cell, see Appendix C, we set $\rho=5.5$ according to the value obtained in the simulations of morphogenesis [15]. The parameter σ^{F} is the linear density of energy at cell-wound boundaries and thus gives the magnitude of the tension of the boundaries. The tension of cell-cell boundaries is considered to be caused by actin filaments pasted along both apical insides of cells. At the cell-wound boundaries, actin filaments are in the cell side but absent in the wound side, and thus the tension is deemed to be half that at cell-cell boundaries, $\sigma^{\mathrm{F}}=0.5$ in the new unit. Since σ^{B} governs wound closure its value was determined by computer simulations under the following two conditions, namely, that wound closure is ultimately completed and that smooth changes are made in the wound margins under closure. The first condition gives the parameter's lower limit, while the second gives its upper limit. For our purposes, we use two different values which satisfy the given conditions, $\sigma^{\mathrm{B}}=3.0$ in simulation A and $\sigma^{\mathrm{B}}=2.0$ in simulation B. It should, however, be noted that the above three parameters need to be determined by more systematic simulations and by comparison with experiments in the future. Here, we should point out that in our simulations, the cell-wound interfacial tension alone is not able to close the wound under the condition $\sigma^{\mathrm{F}}<1$ in the new unit without the cell–basal-lamina adhesion, as mentioned in Sec. I.

B. Snapshots of wound closure

We performed computer simulations using the vertex dynamics cell model for wound closure described in the previous sections. Five simulation runs were carried out using different initial states of wounds, created from an equilibrium state with 100 cells obtained in our past simulations of morphogenesis [15], by changing the number of cells removed, between 16 and 25, and the shape of the wound. Our simulation method is given below. Using the Runge-Kutta-Gill method, we solve the simultaneous ordinary differential equations of the first order Eq. (12) and determine the positional vectors of vertices at each time step, with step size $\delta t(\delta t=0.01)$ and starting from the initial state mentioned above. In this process, we calculate the edge length of every cell at each time step, and if this length is longer than the minimum length $\Delta(\Delta=0.2)$ we proceed to the next step, else we carry out the elementary processes of topological changes T1 and T2 in Figs. 2(a) and 2(b). If a vertex on a wound edge touches another wound edge, we carry out process T3 in Fig. 2(c). Two of our five runs, "simulation A" and "simulation B," are shown below, where all physical quantities are the dimensionless ones defined in Sec. III A and the system is a square of size 10×10 under the periodic boundary condition.

Snapshots obtained from simulation A are shown in Fig. 3 [(1)–(6)]. The gray area in each figure is the wound, while

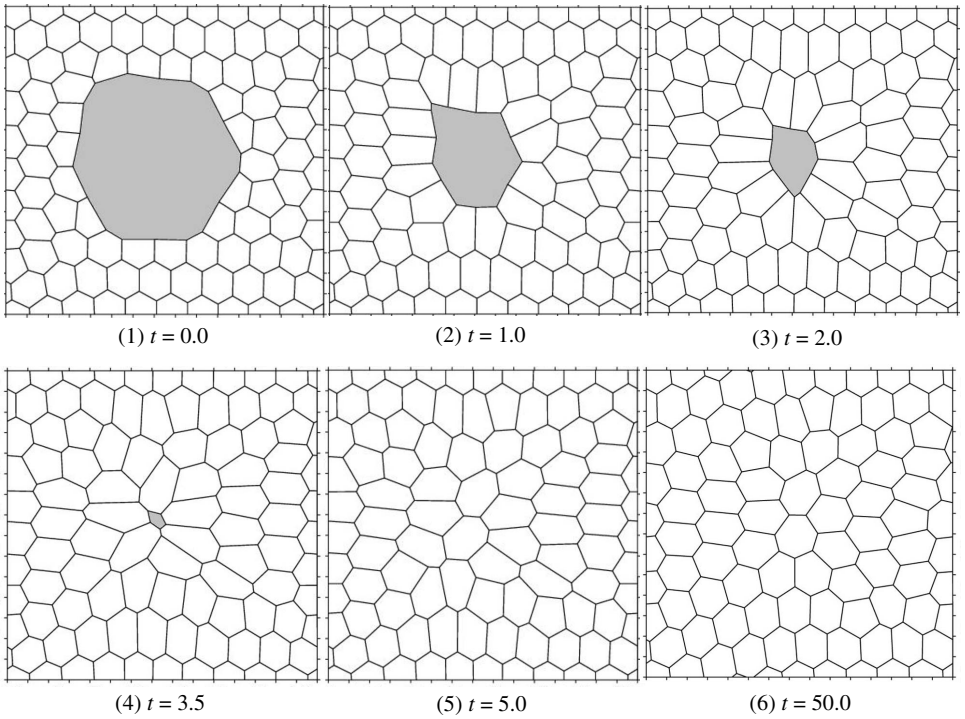

FIG. 3. Snapshots from simulation A during wound closure. The wound (gray area) disappears at $t=3.95$ (dimensionless time). The periodic boundary condition is used.

the surrounding polygons are normal cells. The initial wound, Fig. 3 (1), created by removing 20 cells, is relatively round. As seen in subsequent snapshots, the wound then contracts approximately retaining its initial round shape. During wound contraction, the surrounding cells elongate toward the wound, and the closer to the wound they are, the more they deform. The wound disappears at $t=3.95$ and then the surrounding cells move to decrease the entire length of the cell-cell boundaries as in morphogenesis. The relaxation movements of the cells mostly finish at $t=50.0$ as shown in Fig. 3 (6). We see from the figure that this final state is not much different from the normal-cell part in the initial state, Fig. 3 (1), except for an increase in the average cell area.

Snapshots obtained from simulation B are shown in Fig. 4 [(1)–(6)]. The initial wound, Fig. 4 (1), created from the same original normal state as that in simulation A, is long and narrow. As seen in this figure, the wound contracts and approximately retains its initial shape until a vertex on one long side of the wound margin touches the other side and subsequently splits into two parts according to the adhesion

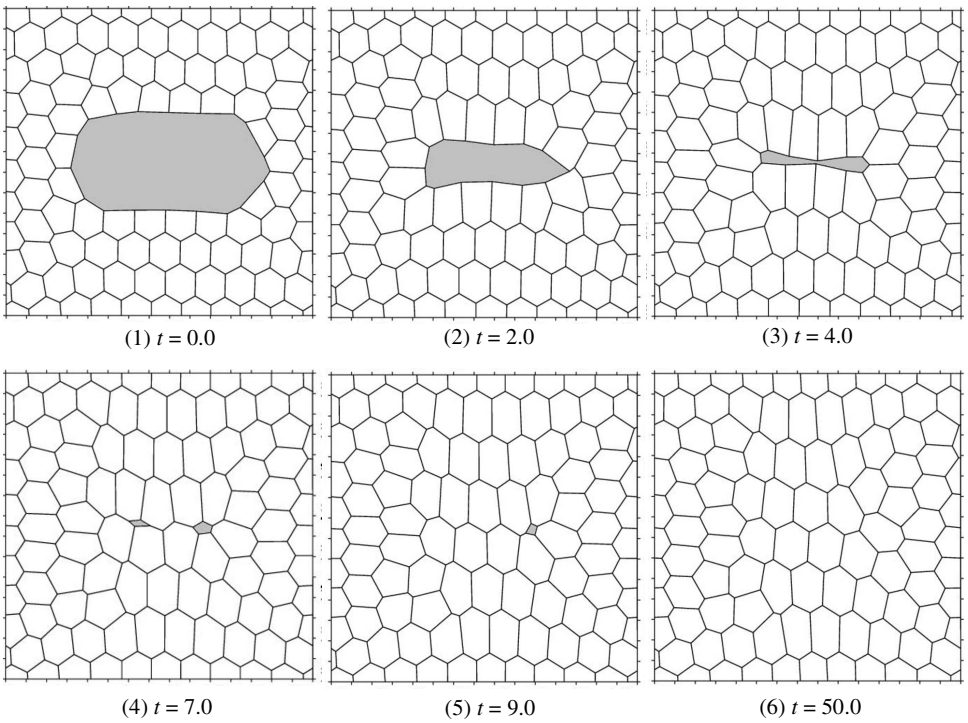

FIG. 4. Snapshots from simulation B during wound closure. The wound (gray area) splits at $t=4.23$ (dimensionless time). The left wound disappears at $t=7.50$ while the right one does so at $t=9.54$. After the wound closure the surrounding cells relax into the final state at $t=50.0$. The periodic boundary condition is used.

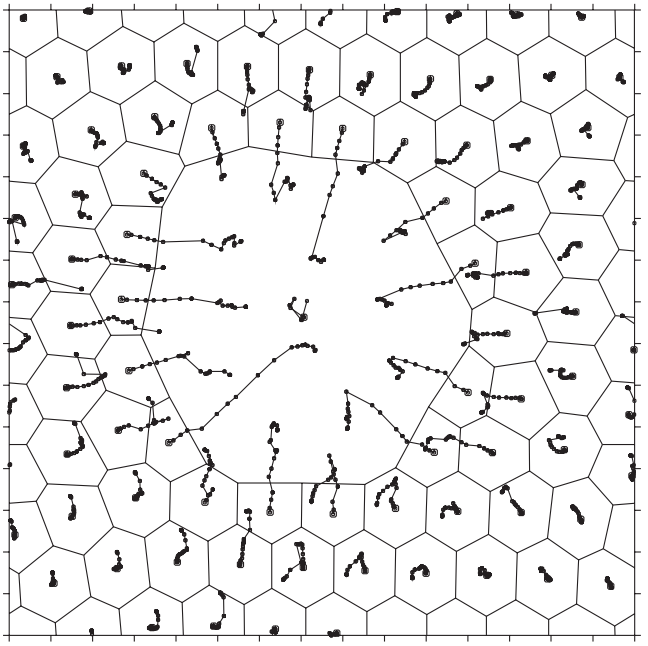

FIG. 5. Motion of the centers of gravity of cells surrounding the wound in simulation A. Loci of the centers of gravity of cells are shown for the period $t=0-200$ of dimensionless time.

process T3 in Fig. 2(c). Thereafter, the two wounds contract individually as shown in Fig. 4 (4), with the wound on the left disappearing at $t=7.50$ and that on the right at $t=9.54$. Finally, as in simulation A, the surrounding cells undergo a relaxation process that almost finishes at $t=50.0$ as illustrated by Fig. 4 (6).

The behavior of the surrounding cells can be seen in Figs. 3 and 4 and is described below. These cells are forced to deform and move by the wound contraction, shifting their center of gravity and elongating toward the wound. After the wound disappears, they slowly change into a roundish shape and finally revert approximately to their normal-cell shape given in the initial state, apart from an increase in the average cell area.

The loci of the centers of gravity of the cells in the initial cellular pattern have been plotted in Fig. 5 for simulation A from $t=0$ to $t=200$, where the locus at the center of the figure denotes that of the center of gravity of the wound. We see from this figure that the surrounding cells move at the same time toward the wound center and that those at the wound margin have much longer loci than others. At about the time that the wound disappears, the loci bend sharply showing the rearrangement of the cell positions. This behavior of the surrounding cells has also been observed in the wounded cat corneal endothelia [4].

C. Contraction process of a wound

Figures 6(a) and 6(b) show the time variation of the wounds in which the contours of the wounds in Figs. 3 and 4, respectively, are superposed. Time t in both figures advances from the outside to the inside.

We see from these figures that the wound margins translate toward the wound center and vanish in turn in the wound contraction process. In other words, the edges of the wound polygon make approximately parallel displacements and then when one of them reaches Δ the number of the wound edges decreases by one according to the T1 process during wound contraction. The new wound polygon repeats the same process while almost retaining its shape. In the case of simulation B, two wound edges touch causing the wound to split into two. After splitting, the two wounds continue the contraction process mentioned above independently.

We now note that Fig. 6(b) closely resembles the superposition of wound contours, Fig. 2 in Ref. [5], and which were obtained by tracing the microscope pictures filmed during wound closure in a *Xenopus laevis* tadpole fin [3]. Furthermore, the recent histological study of wound closure in *Xenopus laevis* embryos has identified the time variation in wound contours using video tape recording. Figure 8 in Ref. [6] shows a remarkable similarity to our results, Figs. 6(a) and 6(b), especially with respect to the fact that the wound contracts while almost maintaining its initial shape.

Figure 6(b) reminds us of the formation of an entrenched meander, a river that meanders in a deep valley [19]. When a free meander in a plain is subjected to land uplift or falls in the base level, erosion of the land occurs once again. If this erosion is mainly vertical, an entrenched meander is formed keeping the meandering pattern and creating almost symmetric banks. The resulting land figure is similar to the right or

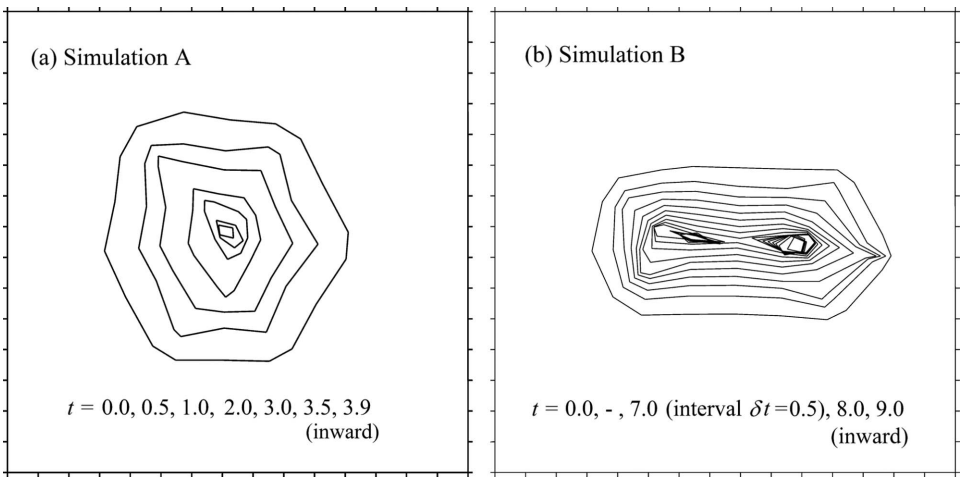

FIG. 6. Contraction process of a wound. The wound contours at each time t in simulation A and simulation B have been superposed in Figs. 6(a) and 6(b), respectively.

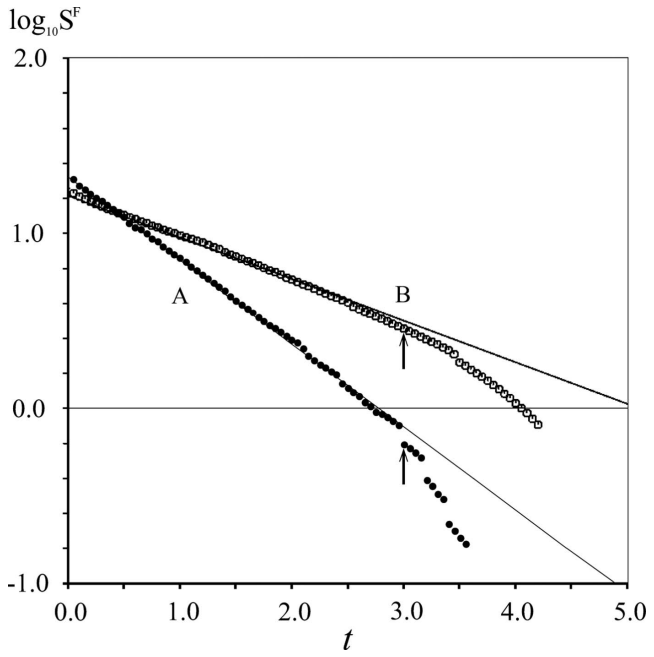

FIG. 7. Time dependence of wound area. The ordinate is the common logarithm of the dimensionless wound area S^F expressed in the unit $S_0=R_0^2$ (the initial average cell area), while the abscissa denotes dimensionless time t. The black and white circles A and B are the results of simulation A and simulation B, respectively, and the straight line accompanying each is its regression line. The arrows in the figure show the time, $t=3.0$, when the decrease in wound area begins to deviate from exponential behavior.

the left half of Fig. 6(b). The two processes in the land figure formation and wound contraction are remarkably similar, if one equates the eroded land to the wound and reverses the time direction. Thus, we can say that wound closure is a reverse erosion process in a wound by marginal cells. In fact, the surrounding cell assembly forms cellular flows toward the wound center and covers the wound area gradually in the lateral direction similar to the flow of water [4]. The underlying action principles in each of the two phenomena are, however, completely different. The erosion of land is caused by the mechanical action of water flow, whereas the erosion of a wound is caused by the thermodynamic action of surrounding cells.

D. Time dependence of wound area

Figure 7 shows the time variations in the wound areas obtained in simulation A (labeled A) and simulation B (labeled B) by plotting the common logarithm of the wound area $S^F(t)$ versus time t. Both graphs clearly show that the wound area decreases exponentially for the period $t=0$ to 3.0 (arrow), i.e., before showing signs of the disappearance of the wound or the adhesion of the wound margin. This leads to the following expression:

$$S^F(t) = S^F(0)\exp\left(-\frac{t}{\tau_s}\right), \tag{13}$$

where $\tau_s=0.92$ for simulation A and $\tau_s=1.83$ for simulation B. The values of τ_s indicate that the wound closure in simulation A occurs nearly twice as fast as that in simulation B.

E. Quantitative description of the wound shape and its time dependence

We now discuss the time variation in the wound shape more quantitatively. Previously we made a qualitative statement from the snapshots shown in Sec. III B, that the wound contracts in such a way as to maintain approximately its initial shape. For our purpose, we use a moment tensor of the wound about its center of gravity, $\mathbf{M}=(M_{\alpha\beta})$, defined by

$$M_{\alpha\beta} = \frac{1}{S^F}\int_{\text{wound}} d\boldsymbol{r}x_\alpha x_\beta, \quad \alpha,\beta = 1,2, \tag{14}$$

where $\boldsymbol{r}=(x_1,x_2)$ denotes the positional vector with its starting point at the center of gravity of the wound, expressed by orthogonal coordinates (x_1,x_2) and the integration is carried out over the entire area of the wound. Here the center of gravity of the wound is not that of the vertex assembly but of the wound-area continuum. The definition of Eq. (14) is equivalent to the moment of inertia tensor of a plate with uniform density and uniform thickness in the mechanics of an elastic body. The wound shape can be described in terms of a shape factor Φ^F defined as

$$\Phi^F = \sqrt{\frac{M_2}{M_1}}, \tag{15}$$

where M_1 and M_2 are the principal values of the tensor $\mathbf{M}$ given by

$$\begin{pmatrix} M_1 \\ M_2 \end{pmatrix} = \frac{1}{2}[(M_{11}+M_{22}) \pm \sqrt{(M_{11}-M_{22})^2+4M_{12}^2}]. \tag{16}$$

This shape factor Φ^F describes the wound shape as an ellipse with the ratio of the short radius b to the long radius a, $\Phi^F=b/a$. $\Phi^F=1$ denotes a circle and $\Phi^F<1$ a flat ellipse. The ellipse in Newtonian mechanics is called the ellipse of inertia and is used to describe the motion of a rigid body with an arbitrary shape.

We calculated Φ^F at each time step t for both simulation A and simulation B (see Appendix A) and obtained the time dependence shown in Fig. 8. These figures show that both shape factors decrease with linear time dependence over the whole period. The regression lines in Fig. 8 are written as $\Phi^F(t)=-0.074t+0.88$ for simulation A and $\Phi^F(t)=-0.102t+0.508$ for simulation B. These results imply that the wound shape becomes flatter gradually as time advances quantitatively explaining the superpositions of contracting wounds shown in Fig. 6.

IV. COMPARISON WITH EXPERIMENTS

In the preceding sections, we compared our simulation results qualitatively with some experimental ones. Now we compare these quantitatively and estimate the parameters for our model. For this purpose, the experiment with wounded cat corneal endothelia [4] is selected for simulation A and

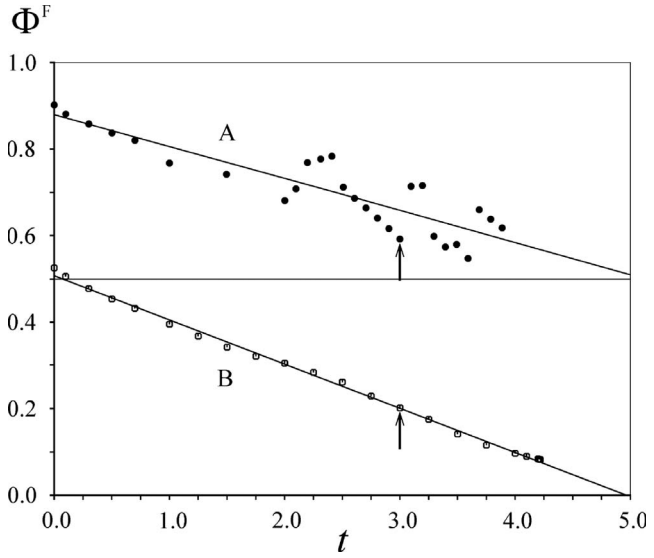

FIG. 8. Time dependence of wound shape factor Φ^F, Eq. (15). The abscissa t denotes the dimensionless time. The black and white circles A and B are the results of simulation A and simulation B, respectively, and the straight line accompanying each is its respective regression line; $\Phi^F(t)=-0.074t+0.88$ for A and $\Phi^F(t)=-0.102t+0.508$ for B. $\Phi^F=1$ depicts a circle and $\Phi^F<1$ a flat ellipse. The arrows show the time, $t=3.0$, at which the decrease in wound area begins to deviate from exponential behavior (see Fig. 7).

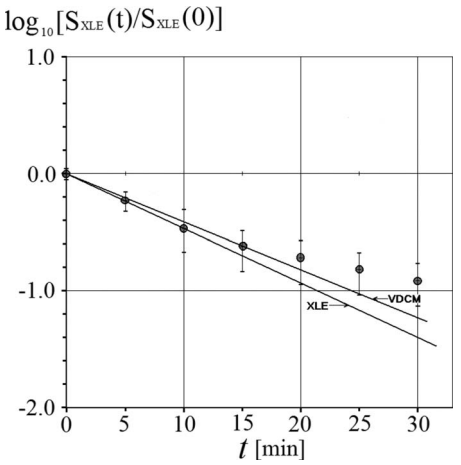

FIG. 9. Time dependence of wound area in *Xenopus laevis* embryos. The ordinate is the common logarithm of the wound area ratio, $S_{XLE}(t)/S_{XLE}(0)$, while the abscissa denotes the time in minutes after wounding. Black circles: experimental results from Ref. [6], where error bars indicate standard deviations. Straight line XLE: fitted to the experimental data in the initial stage with $\tau_{XLE}=9.3$ min. Straight line VDCM: fitted to the simulation B data with $\tau_s=10.6$ min.

that with wounded *Xenopus laevis* tadpole fin [3] for simulation B, because the initial patterns of each are similar. The experimental and simulation data are shown in Table I, where the first row, initial wound size, denotes the number of cells removed from the normal tissue and the last row, disappearance time of wound/initial wound size, denotes the disappearance time of the wound per single cell removed.

If we equate the two corresponding values for disappearance time/initial wound size in the last row, simulation A with cat cornea and simulation B with tadpole fin, we obtain the time units for the respective experimental systems as follows: $\tau_0 \approx 2.8$ days $=2.4\times10^5$ s for cat cornea and $\tau_0 \approx 5.8$ min $=3.5\times10^2$ s for tadpole fin. From these results, we can see that the characteristic time for tadpole fin is about one thousandth that of the cat cornea. In other words, the wound closure in the former case is nearly 1000 times faster than that in the latter. These time units give, in real time unit, the characteristic times for area reduction, τ_s, given in Eq. (13): $\tau_s \approx 2.6$ days for cat cornea and $\tau_s \approx 10.6$ min for tadpole fin. Furthermore, we can determine the quantity η/σ, using the value of τ_0 above and R_0 in Table I with $\tau_0 \equiv \eta R_0/\sigma$, as follows: $\eta/\sigma \approx 0.15$ days/μm $=1.3\times10^{10}$ s/m for cat cornea and $\eta/\sigma \approx 0.29$ min/μm $=1.7\times10^7$ s/m for tadpole fin. We need experimental data of η or σ to proceed further.

We now compare our results for time dependence of the wound area with the experimental ones observed in *Xenopus laevis* embryos. Figure 9 shows the common logarithm of wound area data, $S_{XLE}(t)/S_{XLE}(0)$, versus time t, where $S_{XLE}(t)$ obtained from Fig. 2 in Ref. [6] is the average of the wound areas of the anterior and posterior halves of the embryos at time t. From this figure we can see that the experimental data appear on a straight line with slope $-1/\tau_{XLE}$ for the first 15 min within the error bars. The characteristic time τ_{XLE} is 9.3 min, which is close to the above value for *Xenopus laevis* tadpole fin, $\tau_s \approx 10.6$ min. In fact, drawing a straight line with slope $-1/\tau_s$ we get the straight line VDCM shown in Fig. 9, which is also close to the straight line XLE, though their experimental systems are different from each other.

Our model contains eight parameters $(R_0, h^0, \eta, \sigma, \sigma^F, \sigma^B, \rho, \Delta)$. Consequently, we need eight independent physical

TABLE I. Comparison between simulation and experimental results. Cat cornea: a wound in cat corneal endothelium [4]; tadpole fin: a wound in *Xenopus laevis* tadpole fin [3].

Physical quantities	Simulation A	Simulation B	Cat cornea (Ref. [4])	Tadpole fin (Ref. [3])
Initial wound size (removed cell number)	20	16	180	10
Initial average cell size	R_0	R_0	19 μm	20 μm
Average cell height	h^0	h^0	/	2.4 μm
Disappearance time of wound	$4.0\tau_0$	$4.2\tau_0$	100 days	15 min
Disappearance time of wound/initial wound size	$0.20\tau_0$	$0.26\tau_0$	0.56 days	1.5 min

quantities obtained experimentally to determine all of these. With regard to the above experiments, we need an additional six independent quantities for cat cornea and five for tadpole fin.

It should be noted that the comparisons between our simulations and the two experiments given above are not precise. The disappearance time for a wound in cat cornea given in Table I is taken to be the time at which movement of most cells surrounding the wound terminates, since it is difficult to identify the exact time at which the wound disappears. On the other hand, the time given for tadpole fin in Table I is the exact time at which movement of the cell bodies into the wound stops. The experimental data for tadpole fin, however, include movement of both lamellipodia and cell bodies, whereas our model does not distinguish between these.

In addition, we have assumed in our model that there is no cell division during wound closure and have ignored phenomena appearing in a scale smaller than the minimum length Δ. Our model enables us to understand the mechanism of wound closure in epithelial tissue at the cell level, whereas at the molecule level this appears too complicated. Values of the eight parameters mentioned above can be estimated by a molecule-level study. This situation resembles the relationship between the mechanics of an elastic body and the atomic level study of elastic constants.

V. CONCLUSIONS

In this paper, we investigated through computer simulations how wound closure is performed by surrounding cells and basal lamina without mitotic processes in the case of small wounds using the vertex dynamics cell model of wound closure. Our results are summarized below.

(1) Driving force of wound closure: the primary driving force of wound closure is a force that attempts to decrease the total thermodynamic potential energy of cell–basal-lamina interfaces. The cell-wound interfacial tension is the secondary driving force of wound closure, which assists the primary force to close the wound. Wound closure proceeds as the driving forces overcome resistances due to the two fundamental forces of morphogenesis, cell-cell interfacial potential forces and cell elastic forces.

(2) Behavior of the surrounding cells: our simulations reproduced the following behavior of cells surrounding a wound as observed in wounded cat corneal endothelia [4]. As the wound contracts, the surrounding cells elongate and then at the same time move toward the wound. After the wound disappears they become round and finally cease moving having approximately recovered their initial patterns. The relationships between neighboring cells change during the entire process.

(3) Wound contraction process: the contraction of wound proceeds by repeating the process in which the wound edges translate toward the wound center, and when the shortest edge disappears, the number of wound edges decreases. The wound shape is almost retained during this process. This explains the experimental results in wounded corneal endothelia of cats [4], *Xenopus laevis* tadpole fin [3], and *Xenopus laevis* embryos [6,7]. Furthermore, our model can describe the division of a wound and reproduce the wound closure process accompanied by wound division observed in *Xenopus laevis* tadpole fin [3].

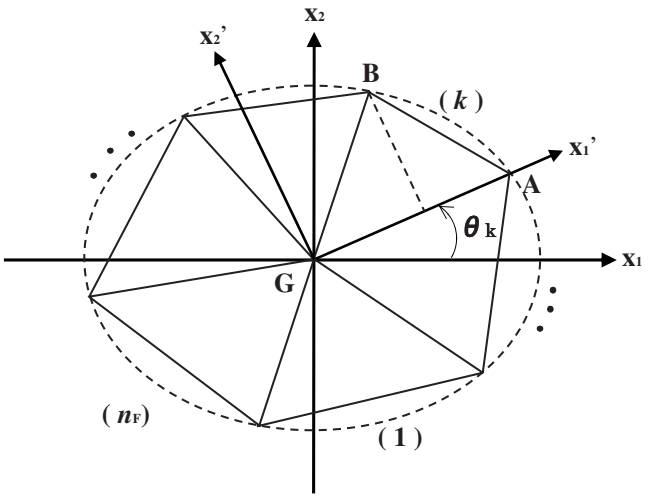

FIG. 10. Calculation of the moment tensor for a polygonal wound with n^F edges. The orthogonal coordinate system G-$x_1'x_2'$ is obtained by rotating the orthogonal coordinate system G-x_1x_2 by angle θ_k about the center of gravity of wound G.

(4) Quantitative description of wound contraction: in order to describe the wound contraction quantitatively we have calculated the wound area and the wound shape factor. The wound area decreases exponentially with its characteristic time. The wound shape can be approximately described as an ellipse and then the wound shape factor is defined as the ratio of the short radius to the long radius of the ellipse. The wound shape factor decreases slowly, linearly with time.

(5) Comparison with experiments: we have compared our simulation results with the results of three experiments for wound closure in cat corneal endothelia [4], *Xenopus laevis* tadpole fin [3], and *Xenopus laevis* embryos [6]. All three experimental results are qualitatively remarkably similar to the simulation ones. To compare these quantitatively, we have determined some values for parameters in the model. We need more experimental data, however, to conduct a more definite quantitative comparison and expect future experiments.

ACKNOWLEDGMENT

The numerical computations presented in this paper were carried out using the VPP700 computer installed at Kyushu University.

APPENDIX A: CALCULATION OF MOMENT TENSORS OF A WOUND

First, we triangulate the wound area by connecting the center of gravity of the wound G with each vertex as shown in Fig. 10. Next, we calculate the moment tensor for each triangle using its analytic expression and then sum these to obtain the moment tensor of wound **M**, Eq. (14).

Writing the moment tensor of the kth triangle about G as $\mathbf{M}'_k$ and the matrix of rotation $G\text{-}x_1x_2 \rightarrow G\text{-}x'_1x'_2$ (angle θ_k) as $\mathbf{T}_k$, we obtain the moment tensor $\mathbf{M}$ in the form

$$\mathbf{M} = \sum_{k=1}^{n^{\mathrm{F}}} {}^t\mathbf{T}_k \, \mathbf{M}'_k \mathbf{T}_k, \tag{A1}$$

$$\mathbf{T}_k = \begin{pmatrix} \cos\theta_k & \sin\theta_k \\ -\sin\theta_k & \cos\theta_k \end{pmatrix}, \tag{A2}$$

$$\mathbf{M}'_k = \frac{1}{6} \begin{pmatrix} a_k^2 + a_k b_k + b_k^2 & c_k\left(\frac{1}{2}a_k + b_k\right) \\ c_k\left(\frac{1}{2}a_k + b_k\right) & c_k^2 \end{pmatrix}, \tag{A3}$$

where n^{F} and ${}^t\mathbf{T}_k$ denote the number of edges of the wound and the transposed matrix of $\mathbf{T}_k$, respectively. The quantities a_k, b_k and c_k in $\mathbf{M}'_k$ are the coordinates of points A and B in the coordinate system $G\text{-}x'_1x'_2$ and are defined as $\mathrm{A}(a_k,0)$ and $\mathrm{B}(b_k,c_k)$, respectively, as illustrated in Fig. 10.

APPENDIX B: SIMPLE PICTURE OF WOUND CLOSURE

In this section, we consider a model that describes the essence of wound closure in terms of the minimum number of elements. For simplicity, we assume a wound to be a regular polygon with n edges. As shown in Fig. 1, the primary driving force acting on vertex i, Eq. (9), always points toward the wound and has a magnitude of $\sigma^{\mathrm{B}} r'_i/2$, where r'_i denotes the distance between two neighbors of i on the wound margin. On the other hand, the secondary driving force acting on vertex i due to the cell-wound interfacial potential, Eq. (7), points toward the wound when the wound is convex at i and has a magnitude of $2\sigma^{\mathrm{F}} \cos(\omega_i/2)$, where ω_i denotes the internal angle of the wound at i. The other forces, i.e., the fundamental forces of morphogenesis, act mainly to resist the wound closure. The primary driving force among these must dominate the wound closure to explain the experimental facts, as mentioned in Sec. I. Therefore, we assume the inward normal velocity of an edge with length r, v, to be

$$v = \mu^* r, \tag{B1}$$

where μ^* is a positive constant that also includes implicitly the effects due to the other forces. The area of this wound, S_n, can be written as

$$S_n = \beta r^2, \quad \beta \equiv \frac{n}{4}\cot\left(\frac{\pi}{n}\right). \tag{B2}$$

Using Eqs. (B1) and (B2), we have the time rate of change of the wound area given by

$$\frac{dS_n}{dt} = -nrv = -\frac{n\mu^*}{\beta} S_n. \tag{B3}$$

The solution to Eq. (B3) is obtained as

$$S_n = S_n(0)\exp\left(-\frac{t}{\tau_s}\right), \quad \tau_s \equiv \frac{1}{4\mu^*}\cot\left(\frac{\pi}{n}\right), \tag{B4}$$

where $S_n(0)$ denotes the initial wound area and τ_s the characteristic time which gives the criterion for the time period of wound closure. Equation (B4) agrees with the simulation result given by Eq. (13). We apply this picture of wound closure to the initial state of simulation A, Fig. 3 [(1) $t=0.00$], regarding it as an approximately regular polygon. Substituting $n=18$ and $\tau_s=0.92\tau_0$ given below Eq. (13) into τ_s in Eq. (B4), we obtain $\mu^*=1.6/\tau_0$. This means that the wound margin moves a distance of about one edge length in τ_0. Wound closure in the case of a regular polygon proceeds with the parallel displacement of each wound margin without a reduction in the number of edges, showing a completely similar contraction.

APPENDIX C: DETERMINING MODEL PARAMETERS FROM ELASTIC CONSTANTS OF A CELL

The main purpose of this section is to show a method for determining parameters in our model from the elastic constants of a cell. The parameter values estimated here should be interpreted as those giving their orders of magnitude, because experimental data measured both *in vivo* and *in vitro* are used. We now consider the thermal elasticity of a prismatic cell with base area S and height h^0 in a fluid medium. Its elastic potential energy u_{D} can be written from Eq. (4) as

$$u_{\mathrm{D}} = \rho(V - V^0)^2, \tag{C1}$$

where $V=Sh^0$ and $V^0=S^0h^0$ are the cell volume and its equilibrium value, respectively. Then the pressure p is given by

$$p = -\left(\frac{\partial u_{\mathrm{D}}}{\partial V}\right)_{is} = -2\rho(V - V^0), \tag{C2}$$

where the subscript is denotes the isothermal change. We assume that the wound closure proceeds in an isothermal process and that all elastic constants given below are measured in the isothermal processes and hence will not refer to this hereafter. Equation (C2) gives the bulk modulus K as

$$K = -V^0\left(\frac{\partial p}{\partial V}\right)_{is} = 2V^0\rho, \quad \text{or} \quad \rho = \frac{K}{2V^0}. \tag{C3}$$

On the other hand, the bulk modulus K is related to the shear modulus G from the general relationship between elastic constants as follows:

$$K = \frac{2(1+\sigma_{\mathrm{P}})}{3(1-2\sigma_{\mathrm{P}})} G, \tag{C4}$$

where σ_{P} is Poisson's ratio.

The dynamic shear moduli of three protein filaments, the cytoskeletons, were measured using rheologic methods *in vitro* [14]. These showed only minimal frequency dependence in the range between 0.01 and 100 rad/s. From this we can argue that the difference between the isothermal shear modulus and the adiabatic one is not so large. Furthermore, the stress-strain curves thereof showed that the actin filament

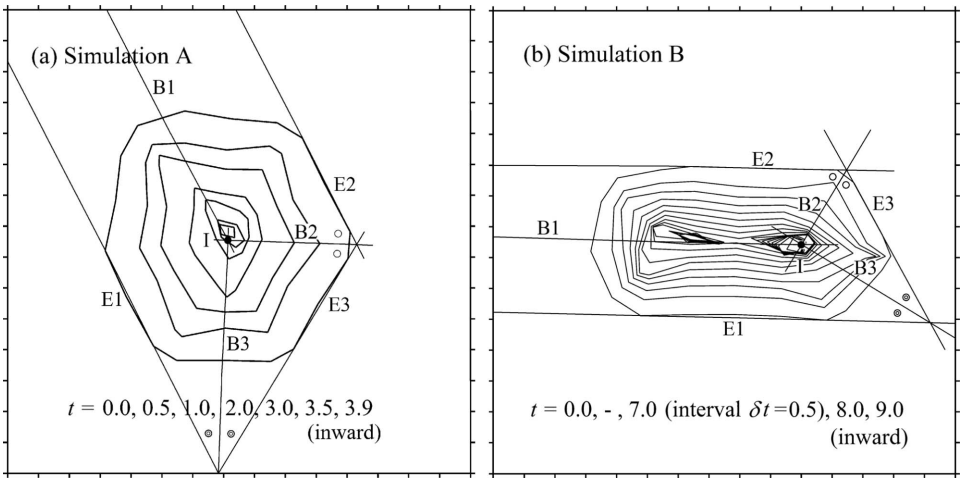

FIG. 11. Prediction of wound disappearance position. The predicted disappearance position of a wound is the incenter of the triangle composed of the longest three edges (E1, E2, and E3) in the initial wound.

had the widest elastic range of stress and the smallest strain for the same stress among the three protein filaments. Therefore, we can consider that the actin filament contributes mostly to the elastic potential energy, Eq. (C1), and thus use the shear modulus of actin filament (concentration 2 [mg/ml]) obtained in the experiment, $G=20.3$ $(\mathrm{N/m^2})$ from Fig. 1 of Ref. [14]. Substituting this value of G into Eq. (C4) we obtain the bulk modulus K as

$$K = 13.5\frac{1+\sigma_P}{1-2\sigma_P}(\mathrm{N/m^2}). \tag{C5}$$

We now estimate values for the model parameters corresponding to the *Xenopus laevis* tadpole fin used in Ref. [3] using the experimental data in Table I and the model parameters in simulation B, $\tilde{\rho}=5.5$ and $\tilde{\sigma}^B=2.0$. Substituting $V^0=R_0^2h^0=9.6\times10^{-16}$ $(\mathrm{m^3})$ obtained from the data of tadpole fin in Table I and Eq. (C5) into Eq. (C3) we obtain the parameter ρ given by

$$\rho = 7.03\times10^{15}\frac{1+\sigma_P}{1-2\sigma_P}\ (\mathrm{N/m^5}). \tag{C6}$$

Using this ρ, $\tilde{\rho}$ and $\tilde{\sigma}^B$ for the definitions, Eq. (10), we obtain the following two parameters:

$$\sigma = 5.89\times10^{-11}\frac{1+\sigma_P}{1-2\sigma_P}\ (\mathrm{J/m}),$$

$$\sigma^B = 5.89\times10^{-6}\frac{1+\sigma_P}{1-2\sigma_P}\ (\mathrm{J/m^2}). \tag{C7}$$

If the inequality $0<\sigma_P<1/2$ also holds in the case of biological cells as in elastic bodies, then the factor $(1+\sigma_P)/(1-2\sigma_P)$ in the above expressions is greater than 1 and hence we have $\rho>7.03\times10^{15}$ $(\mathrm{N/m^5})$, $\sigma>5.89\times10^{-11}$ $(\mathrm{J/m})$, and $\sigma^B>5.89\times10^{-6}$ $(\mathrm{J/m^2})$.

APPENDIX D: PREDICTION OF DISAPPEARANCE POSITION OF A WOUND

We can predict a final disappearance position of a wound from an initial wound polygon by applying the picture of wound contraction shown in Sec. III C. Figures 11(a) and 11(b) show the method for simulation A and for simulation B, respectively.

In the case of Fig. 11(a), we first select the longest three edges (E1, E2, and E3) of the initial wound and then draw three bisectors (B1, B2, and B3) of the internal angles of the triangle composed of the three edges to find its incenter I. The incenter I is the disappearance position of the wound predicted from the initial wound. Although edges E1 and E2 are parallel and do not intersect in this case, the other two bisectors B2 and B3 intersect at incenter I. The straight line B1 equidistant from edge E1 and edge E2 also passes through incenter I. Since the wound disappears at $t=3.95$ near the smallest wound at $t=3.90$ in the figure, the predicted disappearance position I is close to this actual position. In the case of Fig. 11(b), although we have two wound disappearance positions, the above method gives rise to one disappearance position I which predicts the later disappearance position on the right. Since the wound disappears at $t=9.54$ near the smallest wound at $t=9.00$ on the right of the figure, the predicted disappearance position I is close to this actual position.

Although we predicted the disappearance position using the initial wound in the example above, we can use the state of the wound at any time instead of the initial state. We can also use the excenter of the triangle comprising the longest three edges instead of its incenter. The predicted disappearance position is the point in the wound between the incenter and the excenter.

[1] J. Bereiter-Hahn, in *Biology of the Integument*, edited by J. Bereiter-Hahn, A. G. Matoltsy, and K. S. Richards (Springer-Verlag, Berlin, 1986), Vol. 2, Chap. 23, pp. 443–471.
[2] P. O. Seglen and R. Gjessing, J. Cell Sci. **34**, 117 (1978).
[3] G. P. Radice, Dev. Biol. **76**, 26 (1980).
[4] H. Honda, Y. Ogita, S. Higuchi, and K. Kani, J. Morphol. **174**, 25 (1982).
[5] H. Honda, Int. Rev. Cytol. **81**, 191 (1983).
[6] Y. Yoshii, M. Noda, T. Matsuzaki, and S. Ihara, Dev., Growth Differ. **47**, 553 (2005).
[7] Y. Yoshii, T. Matsuzaki, H. Ishida, and S. Ihara, Dev., Growth Differ. **47**, 563 (2005).
[8] R. A. Fisher, Proc. Annu. Symp. Eugen. Soc. **7**, 355 (1937).
[9] J. A. Sherratt and J. D. Murray, Proc. R. Soc. London, Ser. B **241**, 29 (1990).
[10] R. T. Tranquillo and J. D. Murray, J. Surg. Res. **55**, 233 (1993).
[11] P. D. Dale, P. K. Maini, and J. A. Sherratt, Math. Biosci. **124**, 127 (1994).
[12] K. Takamizawa, S. Niu, and T. Matsuda, J. Biomater. Sci., Polym. Ed. **8**, 323 (1997).
[13] U. Savla, L. E. Olson, and C. M. Waters, J. Appl. Physiol. **96**, 566 (2004).
[14] P. A. Janmey, U. Euteneuer, P. Traub, and M. Schliwa, J. Cell Biol. **113**, 155 (1991).
[15] T. Nagai and H. Honda, Philos. Mag. B **81**, 699 (2001); we here presented a model which described morphogenesis of epithelial tissues and performed computer simulations. Equations of motion for vertices in the model are obtained by setting $\sigma^{F}=0$, $\sigma^{B}=0$ in Eq. (12).
[16] B. Alberts, D. Bray, J. Lewis, M. Raff, K. Roberts, and J. D. Watson, *Molecular Biology of the Cell*, 3rd ed. (Garland Publishing Inc., New York, 1994).
[17] A brief explanation of our model and a part of our results have been given in the following paper: T. Nagai and H. Honda, WSEAS Transactions on Biology and Biomedicine **3**, 389 (2006).
[18] K. Kawasaki, T. Nagai, and K. Nakashima, Philos. Mag. B **60**, 399 (1989).
[19] D. L. Holmes, *Holmes Principles of Physical Geology by Arthur Holmes*, 3rd ed. (Thomas Nelson and Sons Ltd., U.K., 1978).